J Appl Physiol 106: 784–795, 2009.
First published January 8, 2009; doi:10.1152/japplphysiol.90376.2008.

Creation of a standardized geometry of the human nasal cavity

Y. Liu,[1] M. R. Johnson,[1] E. A. Matida,[1] S. Kherani,[2] and J. Marsan[2]

[1]*Department of Mechanical and Aerospace Engineering, Carleton University, Ottawa;* [2]*Department of Otolaryngology, Ottawa Civic Hospital, Ottawa, Ontario, Canada*

Submitted 7 March 2008; accepted in final form 1 January 2009

Liu Y, Johnson MR, Matida EA, Kherani S, Marsan J. Creation of a standardized geometry of the human nasal cavity. *J Appl Physiol* 106: 784–795, 2009. First published January 8, 2009; doi:10.1152/japplphysiol.90376.2008.—A novel, standardized geometry of the human nasal cavity was created by aligning and processing 30 sets of computed tomography (CT) scans of nasal airways of healthy subjects. Digital three-dimensional (3-D) geometries of the 60 single human nasal cavities (30 right and 30 mirrored left cavities) were generated from the CT scans and measurements of physical parameters of each single nasal cavity were performed. A methodology was developed to scale, orient, and align the nasal geometries, after which 2-D digital coronal cross-sectional slices were generated. With the use of an innovative image processing algorithm, median cross-sectional geometries were created to match median physical parameters while retaining the unique geometric features of the human nasal cavity. From these idealized 2-D images, an original 3-D standardized median human nasal cavity was created. This new standardized geometry was compared against the original geometries of all subjects as well as limited existing data from the literature. The new model has potential for use as a geometric standard in future experimental and numerical studies of deposition of inhaled aerosols, as well as for use as a reference during diagnosis of unhealthy patients. The specific procedure developed could also be applied to build standard nasal geometries for different identifiable groups within the larger population.

nasal airway; nostril; median nasal geometry; average nasal passageway; processing CT scans

TRADITIONALLY, MEDICATION in the form of drops or aerosols has been delivered to the nasal cavity in the treatment of allergies and congestion. More recently, mainly due to developments in safer and better tolerated enhancers to improve medication absorption by the nasal mucosa, the nasal tract has been considered for the delivery of vaccines, insulin, and other medications to treat osteoporosis, blood disorders, and migraine headaches (18, 29). Despite the growing interest in nasal drug delivery systems (15, 32), the pharmaceutical industry does not have a standard nasal replica for testing devices using aerosol medication, which is typically delivered either as metered-dose liquid sprays or as a dry powder. Most in vitro studies that have appeared in the literature (e.g., 8, 20, 23) used realistic replicas of particular individuals, and thus lack universality. Those geometries may not properly represent the population in general when aerosol medication deposition is concerned.

To optimize the delivery of therapeutic aerosols, a full understanding of particle deposition patterns in the human nasal cavity is necessary through experimental (both in vitro and in vivo) and numerical studies of aerosol deposition. Several experimental studies (e.g., 6–8, 20, 23, 56) and numerical investigations using computational fluid dynamics (CFD; e.g., Refs. 19, 22, 28, 45, 47, 54, 57) have appeared in the literature, but nasal drug delivery remains a poorly understood problem due in large part to the complexity of the human nasal cavity geometry.

The highly complex geometry of the human nasal cavity is not only an obstacle in the research of nasal drug delivery, but also raises significant challenges in clinical research in many related fields including nasal surgery (e.g., 1, 33, 34, 36, 39, 44, 58), nasal toxicology (e.g., 3, 24, 25, 35, 41, 46, 54, 57), risk assessment (e.g., 40, 42, 55), disease diagnosis (e.g., 12, 26, 37, 51), and olfaction (e.g., 9, 11, 59). The creation of a standardized three-dimensional geometry of the human nasal cavity representative of the general population, as well as a procedure for developing geometries of specific population subsets, would be a significant development that could benefit all of these fields.

Although other investigations have measured basic characteristic dimensions of the human nasal cavity using acoustic rhinometry (AR; Refs. 6, 10, 17, 21, 31, 53), magnetic resonance imaging (MRI; Refs. 6, 7, 10, 16), computed tomography (CT; Refs. 31, 53), and an in vivo cast (52), none have attempted to determine a median human nasal geometry. Table 1 summarizes the measurements taken in these studies along with number of subjects and techniques used.

Kesavanathan and Swift (21) measured the characteristic dimensions of the nostrils of 10 healthy Asian and European American subjects aged 23–60 yr using AR. Three nostril shape measurements were taken: the major axis of the nostril cross-section (the length of the nostril), the minor axis of the nostril cross-section (the width of the nostril), and the angle of the major axis with the base of the nose (i.e., the complement of the half angle between the major axes of the nostrils in the inlet plane). These data were used to augment the current data when defining a generic nostril inlet plane in the present study. Several of the other studies listed (e.g., 10, 17, 31, 53) were primarily concerned with demonstrating the AR technique for estimating flow cross-sectional areas (CSA) and comparing its accuracy with more precise MRI and CT measurements. The reported CSA data from all of the works listed in Table 1 were used as a reference for comparison with the standardized geometry developed in this paper.

The objectives of this study were to summarize geometric characteristics of the nasal cavities of 30 healthy adults; to develop an objective methodology for aligning, scaling, and averaging the associated 60 single individual nasal passages; and to use this methodology to create a single, detailed,

Address for reprint requests and other correspondence: M. R. Johnson, Mechanical and Aerospace Engineering, Carleton Univ., 1125 Colonel By Drive, Ottawa, ON, Canada (e-mail: Matthew_Johnson@carleton.ca).

The costs of publication of this article were defrayed in part by the payment of page charges. The article must therefore be hereby marked "*advertisement*" in accordance with 18 U.S.C. Section 1734 solely to indicate this fact.

 8750-7587/09 $8.00 Copyright © 2009 the American Physiological Society

Downloaded from http://jap.physiology.org/ by 10.220.33.5 on January 25, 2017

Table 1. *Characteristic dimensions of human nasal cavity measured by others*

Researchers and Year	Number, Gender (M/F), and Age of Subjects	Method	Reported Measurement Data	Focus of Paper
Hilberg et al., 1989 (17)	6, 3/3, 22–55 yr	AR	CSA as a function of distance for both left and right nasal cavities	Assessed AR technique for measuring CSA of the nasal cavity as a function of the distance from the nostril.
Min and Jang., 1995 (31)	30, 22/8, 20–62 yr	AR and CT scans	CSA as a function of distance for both left and right nasal cavities	Evaluate the validity and characteristics of AR tests compared with the results obtained from CT scans.
Swift and Kesavanathan, 1996 (52)	1, 1/0, N/A	In vivo casting	CSA, perimeter, and hydraulic diameters of 11 cross sections	Use fibrous filter theory to determine the deposition efficiency in nasal cavity.
Cheng, Y. S. et al., 1996 (7)	4, 4/0, 36–57 yr	MRI	CSA, total surface area, and perimeter of cross sections	Experiments on deposition of ultrafine particles in human nasal cavity and its relationship to airway geometry.
Cheng, K. H. et al., 1996 (6)	10, 10/0, 24–58 yr	MRI and AR	Minimum CSA, surface area, and defined "shape complexity"	Deposition efficiency in terms of nasal shape parameters
Corey et al., 1997 (10)	5, 3/2, N/A	AR and MRI	CSA and volume as a function of distance	Determine accuracy of AR as a technique in assessing nasal CSAs and volumes by comparing with MRI.
Guilmette et al., 1997 (16)	45, 21/24, N/A	MRI	Total surface area and internal volume	Correlations for nasal area and volume with measured body parameters
Kesavanathan and Swift, 1998 (21)	10, 7/3, 23–60 yr	AR	Nostril shape (characteristic dimensions)	Effect of particle size, flow rate, nostril shape and nasal passage geometry on nasal particle deposition efficiency.
Terheyden et al., 2000 (53)	6, 3/3, 22–55 yr	CT scans and AR	Comparison of CSA-distance curve using CT scans and AR	Validate the AR technique against CT scanning.

AR, acoustic rhinometry; CT, computed tomography; CSA, cross-sectional area.

standardized geometry that could be considered as a standard human nasal cavity for aerosol deposition studies (experimental and numerical). The described methodology has potential for future work to develop specific models for population subsets.

Anatomy and Physiology of Nasal Cavity

While the human nasal cavity is highly variable among individuals, it does retain several key features. The nasal cavity is nominally symmetric and is separated into two distinct air passages by a vertical thin wall called the nasal septum. The top part of the nasal cavity is formed by bones and cartilage and is tent shaped. The floor of the nasal cavity is formed by the palate, which separates the nasal and oral cavities and extends horizontally toward the posterior of the skull. As shown in Fig. 1, there are three shelves on the lateral wall known as turbinates or conchae, which serve to increase the surface area exposed to the air, thus increasing heat and moisture exchange. The grooved space below each turbinate is referred to as a meatus. The turbinates and meatuses are each labeled superior, middle, or inferior (see Fig. 1*B*).

In the nasal vestibules, the regions just after the nostrils, numerous filtering hair follicles and sebaceous glands are present (38). In the superior region of the nasal cavity, the walls are covered by olfactory mucosa. The remainder of the nose is lined with respiratory mucosa (containing ciliated epithelium, producing mucus and secreting antibacterial enzymes), which clears the cavity by moving contaminated mucus toward the pharynx (throat) where it is swallowed (30). As a human breathes, inhaled air enters the nasal cavity from the nostril and passes through the narrowest portion of the

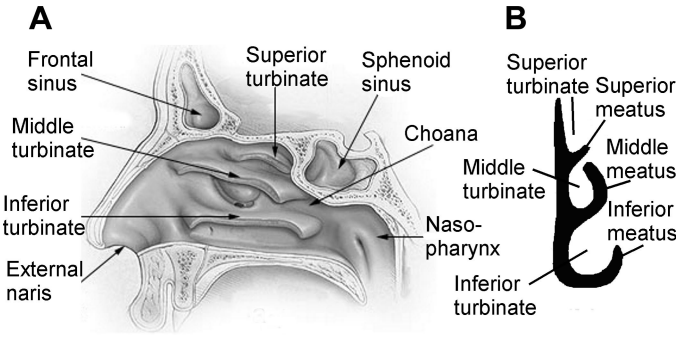

Fig. 1. Anatomy of the human nasal cavity schematic of a sagittal plane cut (*A*) and sample coronal plane midway through the nasal cavity (*B*).

Downloaded from http://jap.physiology.org/ by 10.220.33.5 on January 25, 2017

nasal cavity, i.e., the nasal valve, which increases its speed (14). The air then expands and decelerates while flowing through the middle and posterior part of the nasal cavity, impinging and circumventing the three turbinates and potentially creating turbulence that promotes contact between the air and the mucosa. With this complex geometry, the nose filters, warms, and humidifies the entering air.

MATERIALS AND METHODS

Generation and Alignment of Individual 3-D Nasal Cavity Models

Converting CT scans to coarse 3-D models. Coronal CT scans for 30 healthy adult subjects were obtained in partnership with the Department of Otolaryngology at the Ottawa Civic Hospital. CT scans were completed as part of the work-up for patients who were ultimately determined to have migraine, cluster, or tension headaches, all of which are not known to have any accepted associated anatomic abnormality. In coordination with the hospital's Ethics Board, the normal scans were obtained while maintaining patient anonymity.

All scans were reviewed and confirmed to have nasal anatomy considered to be within normal limits. Specifically, there were no obstructing lesions and the septum was not deviated. Subjects were not decongested for the imaging. The distance between consecutive slices was 2.5 mm, except in three subjects for which cuts were 1 or 2 mm apart. The age and gender of each subject were recorded as well as the characteristics of CT scans, which are shown in Table 2. The age of subjects ranged from 17 to 78 yr (median of 45); there were 13 men and 17 women. Ethnicity was not specifically tracked as part of the original examinations and thus these data were not available. However, the included scans were indiscriminately chosen to include all available normal scans of patients presenting at the Department of Otolaryngology, and the subjects, who had a variety of ethnic backgrounds, could be expected to comprise an unbiased sample of the Ottawa, Ontario, Canada population [predominantly Caucasian with 16% visible minorities including 4.0% Black, 2.9% Chinese, and 2.5% Arab, as reported by Statistics Canada, 2006 (4)].

Table 2. *Subject and CT scan information for 30 individuals in current study*

Subject No.	Sex	Age	Distance Between Slices, mm	Resolution in *x-y* Plane, mm/pixel	Number of Scan Planes
1	F	45	2.5	0.325	38
2	M	59	2.5	0.325	40
3	F	63	2.0	0.24	39
4	F	36	2.5	0.325	38
5	F	20	2.5	0.325	40
6	F	49	2.0	0.325	36
7	F	30	2.5	0.325	32
8	M	74	2.5	0.325	43
9	M	60	2.5	0.325	42
10	F	17	2.5	0.325	39
11	M	56	2.5	0.325	40
12	M	52	2.5	0.325	44
13	M	39	2.5	0.325	40
14	F	37	2.5	0.325	38
15	M	52	2.5	0.3	43
16	M	41	2.5	0.293	39
17	F	78	2.5	0.339	43
18	F	26	2.5	0.245	41
19	M	52	2.5	0.283	42
20	F	23	2.5	0.313	44
21	M	52	2.5	0.325	39
22	F	45	2.5	0.325	34
23	F	52	2.5	0.325	38
24	F	30	2.5	0.325	45
25	F	34	2.5	0.325	41
26	F	66	1.0	0.348	80
27	F	49	2.5	0.325	42
28	M	36	2.5	0.325	40
29	M	42	2.5	0.293	47
30	M	45	2.5	0.293	40
Average		45.3	2.42	0.315	41.6
Median		45	2.5	0.325	40
Max		78	2.5	0.348	80
Min		17	1	0.24	32

M, male; F, female.

The raw 2-D CT images were first processed using 3D-Doctor (Able Software, Lexington, MA) to produce coarse, 3-D nasal cavity geometries for each of the subjects. The 30 coarse models (including both left and right nasal airways) were generated from CT scans in a three-step process that included: *1*) importing images and setting calibration parameters (i.e., image resolution and distance between scans), *2*) segmenting images (using the texture-based auto-segmentation function within 3D-Doctor) and processing boundaries, and *3*) rendering surfaces and exporting coarse 3-D models.

It should be noted that the paranasal sinuses (the air-filled pockets located within the bones of the skull surrounding the nasal cavity) were excluded from the model. During processing of the raw CT scans, the paranasal sinuses were easily distinguished from the main nasal passageway and were readily excluded by adjusting the segmenting parameter within the 3D-Doctor software.

Alignment of coarse 3-D models. In general, when CT scans are taken, there is no precise method of positioning subjects or defining a measurement origin, such that the 3-D orientation of each set of CT scans varies. Thus, before direct comparisons or physical measurements could be made, all of the generated coarse 3-D models needed to be rotated and aligned to a commonly defined position. In all, sufficient geometric constraints had to be applied to satisfy six degrees of freedom (3 spatial coordinates, *x, y, z* of a common origin and 3 independent rotation angles about this origin). After much experimentation with the raw CT images and the coarse 3-D models, a multistep procedure was developed to provide the necessary geometric constraints.

The first part of the procedure involved specifying a common "landmark" on each set of CT scans. The tip of the anterior maxillary spine, or the point where the nasal septum intersects the maxilla bone, was chosen as the first landmark (Fig. 2*A*). This location was identifiable within each set of coronal plane CT scans and was representative of the anterior region of the nose. The mean length of the anterior maxillary spine of all 30 subjects was determined to be 6.5 ± 1.9 mm. Thus the uncertainty in defining this location was consistent with the spacing of the CT scans. The landmark was identified on each model and assigned an arbitrary *x-y-z* coordinate location of (0 mm, 0 mm, 0 mm), thus removing three degrees of freedom.

A second constraint was developed by identifying the point on a posterior coronal plane at which the two nasal airways merge, known as the choana or the opening into the nasopharynx (Fig. 2*B*). The imaginary line joining the anterior maxillary spine and the choana was then used to define the nominal plane of symmetry. By rotating the 3-D model about this line until the projected area viewed from the top of the model was minimized, the *x-y* plane of symmetry could be fully specified for each model, thus removing two additional degrees of freedom. With a subsequent rotation about the *y*-axis, the symmetry plane was aligned with the final *X-Y* coordinate plane.

The procedure for rotational alignment is illustrated schematically in Fig. 3, which shows the initial (*x-y-z*) and final, aligned (*X-Y-Z*) coordinate axes of *model no. 8*. The initial rotation about the imaginary reference line linking the maxillary spine landmark and the choana is indicated by the angle α. The secondary rotation about the *y*-axis is given by angle β. Figure 4*A*, *B*, and *C* show rendered images of nasal *model no. 8* before and after the two rotations. In general, the magnitude of the rotational transformations α and β were small since the subjects were approximately aligned prior to taking coronal plane CT scans. In the current data, the maximum rotational corrections, α

Downloaded from http://jap.physiology.org/ by 10.220.33.5 on January 25, 2017

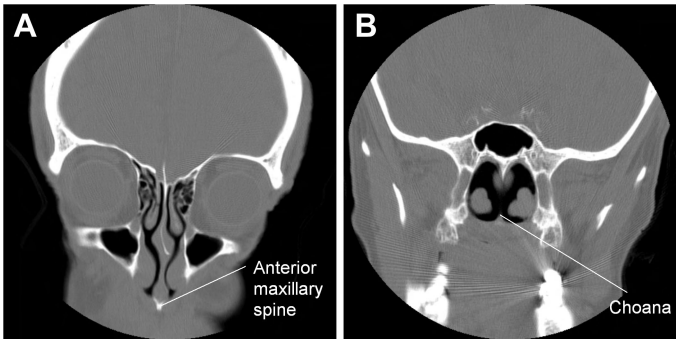

Fig. 2. Identification of the maxillary spine landmark (*A*) and choana (*B*) in the raw, coronal plane computed tomography (CT) scans. Note the apparent rotational misalignment toward the clockwise direction of the raw CT images.

in the coronal (*y*-*z*) plane, and β in the transverse (*x*-*z*) plane, relative to the orientation of the raw CT scans were all between −5.0° and 4.0° and −2.0° and 5.0°, respectively.

A final rotational constraint was applied by rotating the model about an axis perpendicular to the plane of symmetry (*Z*-axis) until the projected area on *y*-*z* plane as viewed from the front of the model was minimized. This rotation is indicated by the angle, θ, in Fig. 3, and is shown by example for *model no. 8* in Fig. 5. θ is a measure of the rotational pitch of each subject's head during the CT scans, which varied more significantly among subjects. For the current data, rotational adjustments of up to 35.5° were necessary to align the models.

This entire alignment procedure was repeated for each of the 30 subjects. With the six degrees of freedom appropriately constrained, the resulting 30 coarse nasal cavity models were aligned so that the location of the common maxillary spine landmark was identically specified, and the direction of the *X*-*Y*-*Z* axes were fixed relative to the nominal plane of symmetry.

Each of the aligned coarse nasal cavity models was divided into three subregions: the anterior/nostril region (from anterior tip of the nostril to the anterior maxillary spine), the middle/nasal airway region (from the maxillary spine to the choana), and the posterior region (corresponding to the region posterior to the choana known as the nasopharynx), as indicated in Fig. 6.

Creation of the Standardized Human Nasal Cavity Model

Measuring characteristic length and scaling the individual coarse models. Prior to attempting to determine a median shape of a standardized 3-D nasal cavity, it was necessary to compensate for size

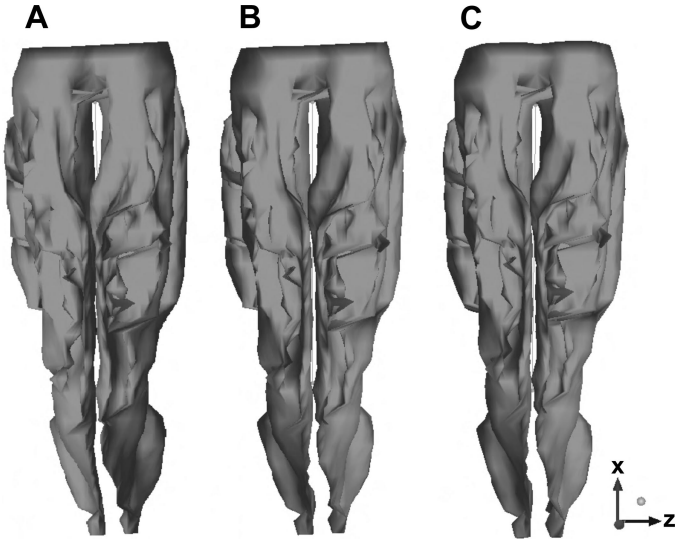

Fig. 4. Example images during rotational alignment of coarse 3-D nasal cavity *model 8*. *A*: top view of model before rotation; *B*: top view of model after rotation around imaginary reference line linking the maxillary spine landmark and the posterior merge point (choana); *C*: top view of model after rotation around *Y*-axis to align symmetry plane with *X*-axis.

variations among subjects. For each subject geometry, a characteristic length of the middle/airway region was defined as the dimension in the *X*-direction between the anterior maxillary spine landmark to the choana or posterior merge point of the nasal airways. As reported in Table 3, the measured characteristic lengths range from 50 to 80.5 mm, which reflects differences in sex as well as normal variability among subjects. However, relative to an average length of 65.1 mm, the standard deviation is only 7.2 mm or 11%.

To facilitate computation of a median 3-D shape, each of the nasal cavity models was geometrically scaled using the ratio of the average characteristic length of all nasal geometries to the characteristic length of that specific geometry:

$$S_i = L_M / L_{M,\,i},$$

where S_i is the geometric scale factor for the *i*th model, $\bar{L}_M = 65.1$ mm and is the averaged characteristic length, and $L_{M,i}$ is the characteristic length of the *i*th model as listed in Table 3. Referring to Table 3, this

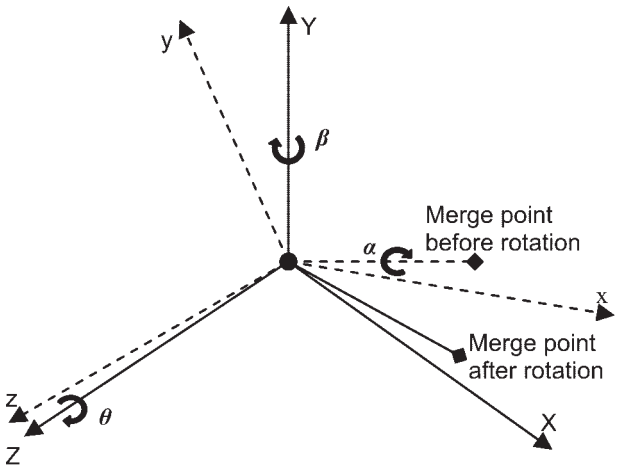

Fig. 3. Coordinate systems before and after rotational alignment of the coarse 3-dimensional (3-D) nasal cavity model.

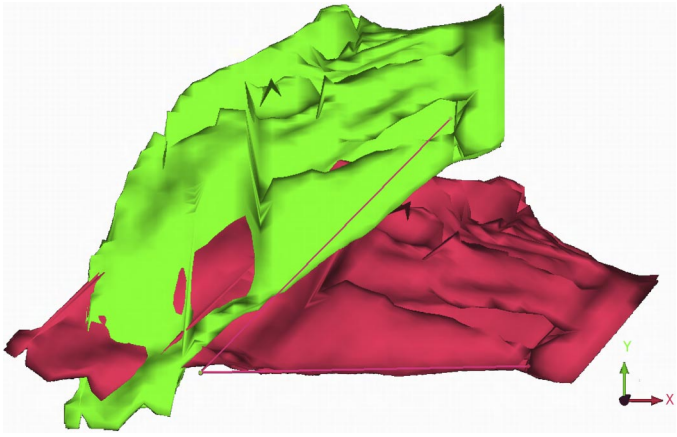

Fig. 5. Lateral view of example images of *model number 8* showing rotational alignment of a coarse 3-D nasal cavity model. Original orientation is shown in green and final aligned model is shown in red. The positions of the imaginary reference lines before and after alignment are indicated.

Downloaded from http://jap.physiology.org/ by 10.220.33.5 on January 25, 2017

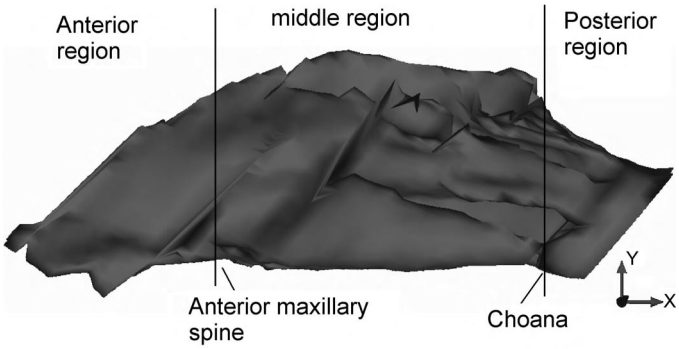

Fig. 6. Separation of a 3-D nasal cavity into three regions.

was generally a small adjustment since most of the scale factors were within 11%, and all were within 24%, of unity.

Slicing and smoothing individual coarse models. Each of the aligned and scaled coarse 3-D models was then sliced by *Y-Z* planes along the *X*-direction using ICEM software (Ansys, Canonsburg, PA) to generate up to 56 coronal plane images spaced 2 mm apart for each of the 30 full nasal models.

As noted previously, the right and left nasal passages of each of the 30 full nasal models in this study were considered as distinct geometries. Thus, in the frontal and middle regions of the model (anterior to the choana), each of the coronal plane images generated from the aligned and scaled models was separated into two distinct images, containing the boundaries of either the left or right nasal passages. The images of the left nasal passages were mirrored about the plane of symmetry (determined using the procedure described above), to produce 30 additional sets of images of right nasal airways. This procedure effectively doubled the available sample size to produce a total sample of 60 sets of right nasal airway coronal plane images.

Since not all of the available sets of CT scans extended fully to the tip of the nose, and in general they terminated at different posterior locations downstream of the choana, fewer than 60 coronal plane images were available toward the anterior and posterior ends of the model. Figure 7 shows a plot of the number of coronal plane images available at each *X*-location along the length of the nasal cavity. The vertical lines on the graph indicate the relative *X*-locations of the entry into the final nasal model (developed below), the anterior maxillary spine, the choana, and the posterior termination of the final model (within the nasopharynx near the pharyngeal wall). Throughout most of the length of the nasal cavity, 60 cross-sectional (coronal) images were available, which included the region of highest geometric variability.

Boundaries obtained from the 56 cross-sectional images of each coarse model were individually checked and smoothed using the ICEM software to eliminate any obvious errors generated from 3D-Doctor, such as discontinuous curves or abnormally sharp or angled edges. The procedure of smoothing included: *1*) manually selecting 60∼100 points along each boundary curve (the number of points

Table 3. *Individual subject measurements*

Subject No.	Sex	Characteristic Length of Middle Region in *X*-Direction, mm	Internal Volume Of Middle Region Of Single Nasal Passage, mm^3		CSA in Middle Region of a Single Passage, mm^2	
			Left	Right	Max	Min
1	F	60.1	10,418	10,509	240	111
2	M	67.6	10,212	11,245	209	68
3	F	50	8,745	7,523	215	118
4	F	56.7	8,934	10,000	307	69
5	F	69.3	6,468	8,075	179	52
6	F	60.8	1,0462	6,782	221	52
7	F	62.9	6,846	7,660	157	67
8	M	66.3	10,862	9,756	275	68
9	M	65.1	10,481	11,880	244	67
10	F	67.9	9,315	8,988	224	71
11	M	64.6	10,980	12,561	238	103
12	M	73.4	11,227	11,827	242	85
13	M	60.1	16,145	13,819	354	82
14	F	60.8	9,971	9,486	230	82
15	M	57.7	8,655	13,601	274	82
16	M	61	7,066	8,111	202	60
17	F	65	10,527	9,331	213	91
18	F	60	7,567	9,104	254	50
19	M	78.3	15,549	14,289	280	78
20	F	65.3	12,099	14,356	296	97
21	M	72.3	12,807	16,192	312	89
22	F	65.6	8,093	7,199	189	59
23	F	63.8	8,346	97,74	194	58
24	F	77.4	11,293	9,285	230	43
25	F	61.2	11,843	12,411	260	102
26	F	53	10,747	10,751	322	83
27	F	66.3	9,127	10,432	236	68
28	M	63.6	9,951	16,435	306	89
29	M	80.5	15,989	11,660	261	66
30	M	76.6	12,283	11,002	223	66
Average		65.1	10,434	10,801	246	76
Median		64.8	10,440	10,471	239	70
SD		7.2	2,458	2,568	46	19
Max		80.5	16,145	16,435	354	118
Min		50	6,468	6,782	157	43

Max, maximum; Min, minimum.

Downloaded from http://jap.physiology.org/ by 10.220.33.5 on January 25, 2017

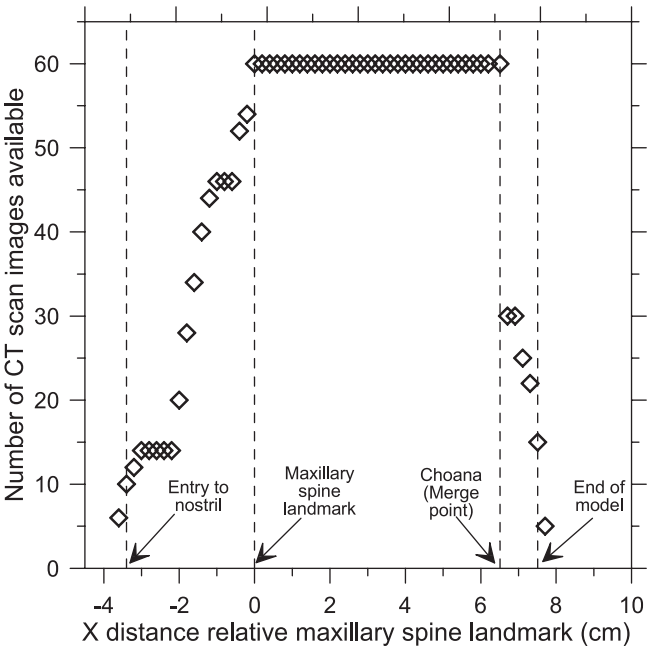

Fig. 7. Number of available coronal-plane images at each *X*-location along nasal cavity.

varied for different length boundary curves), *2*) creating smoothed boundary curves (see Fig. 8) from these points using the automatic curve-generating function within ICEM, which uses the standard B-spline algorithm (13), *3*) exporting a set of 56 new, smoothed cross-sectional (coronal) images for each model, and *4*) rendering a new smoothed 3-D surface from the adjusted coronal images of each single passage using the surface-generating function within ICEM.

Figure 9 shows a set of 36 of the 60 final coronal plane images available at a location 30 mm further into the nasal cavity, relative to the maxillary spine landmark. As is evident in the images, this region has the most dramatic geometric variability of any location along the nasal cavity. While the general structure of the cavity (vertical passage with turbinates) is apparent in each of the images, the exact shape varies dramatically.

Measurement of characteristic dimensions of individual 3-D nasal cavity models. Several measurements, in addition to characteristic length, were taken for each model and are also shown in Table 3. The internal volume of the middle region of each single nasal airway was calculated by summing the products of the CSAs of all coronal planes and the distance between planes (2 mm). Measurements were corrected for scale so that actual physical dimensions are shown. The internal volumes of each single nasal airway (i.e., left/right airway in the middle region) and the minimum and maximum flow CSAs in each airway show significant variability among subjects. Maximum and minimum CSAs for extreme subjects were as much as 55% larger or 43% smaller than average values.

Table 4 summarizes measured dimensions for the anterior/nostril region of the nasal models using the available seven complete sets of scans (representing 14 single nasal passageways) that extended fully to the anterior tip of the nostrils. Calculated internal volumes and surface areas are also included in the table. Similar to the measurement of volume, the surface area of each complete nasal cavity was obtained by summing the products of the perimeters of each coronal plane cross-section and the distance between planes (2 mm). As expected, and consistent with previous studies using other methods (21), there is variability in the length and width of the nostrils as well as the nostril angle (defined as the angle within the entry plane between the major axis of the nostril and the base of the nose). Because of the significant variability throughout the individual nasal cavities, a sophisticated image processing protocol was required to fulfill the goal of generating a meaningful standard cavity model, as described below.

Image processing methodology for generating median coronal plane images. For each of the 56 *X*-locations, the available images were processed to produce a median cross-sectional shape at that location. To aid this process, several in-house algorithms were developed using image-processing tools from LabVIEW (National Instruments, Austin, TX). Through a process of ensemble averaging, thresholding, and edge detection, while considering physical shape and area constraints, these algorithms allowed statistically based estimation of median cross-sectional geometries. Figure 10, *A–D*, shows example images for a coronal plane 30 mm into the cavity in the *X*-direction relative to the maxillary spine landmark at various stages during processing. As noted above, this region of the nasal cavity exhibited the maximum geometric variability and presented the greatest challenge in determining a median shape. The full analysis procedure involved several steps as described below.

1) All available cross-sectional images at each *X*-location were binarized (intensities of pixels located within the boundary were set to unity while pixels outside the boundary were set to zero) and summed (pixel by pixel addition of intensities at corresponding locations in all of the images) to create a single, ensemble averaged grayscale image for each of the 56 *X*-locations in the model. The sample image for $X = 30$ mm is shown in Fig. 10*A*.

2) A "median" image, defined as the pixel by pixel collection of all points that fell within at least 50% of the nasal cavities, was generated from the ensemble averaged, grayscale images. This was accomplished by applying a 50% threshold (i.e., a threshold value equal to one-half of the total number of available images) to produce a binary image where pixels with value 1 fell within at least 50% of cavities and pixels with value 0 did not. A sample median image for $X = 30$ mm is

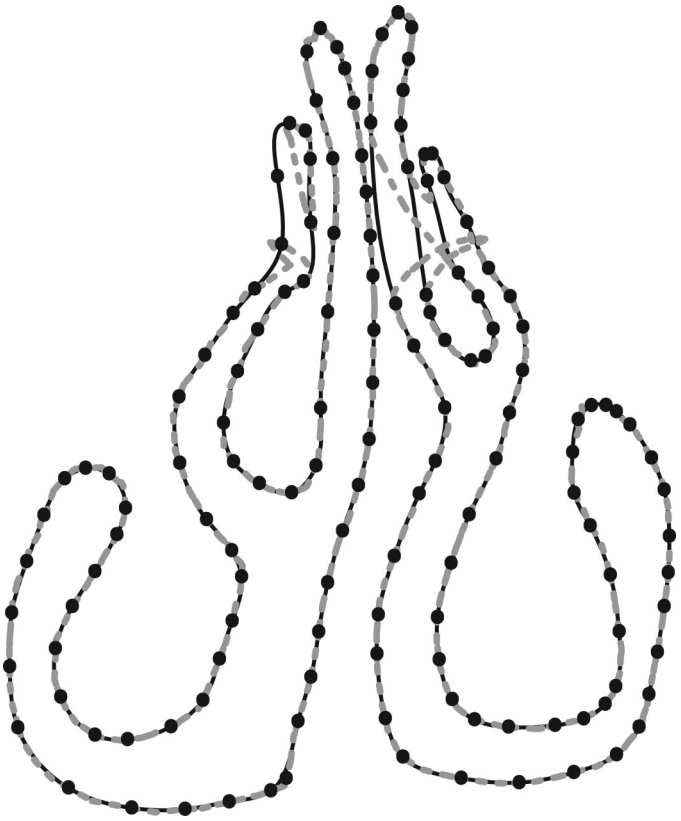

Fig. 8. Example of cross-sectional boundary smoothing. Dashed gray curve is original boundary, points are manually selected on this boundary, and black continuous curve is corrected and smoothed boundary.

Downloaded from http://jap.physiology.org/ by 10.220.33.5 on January 25, 2017

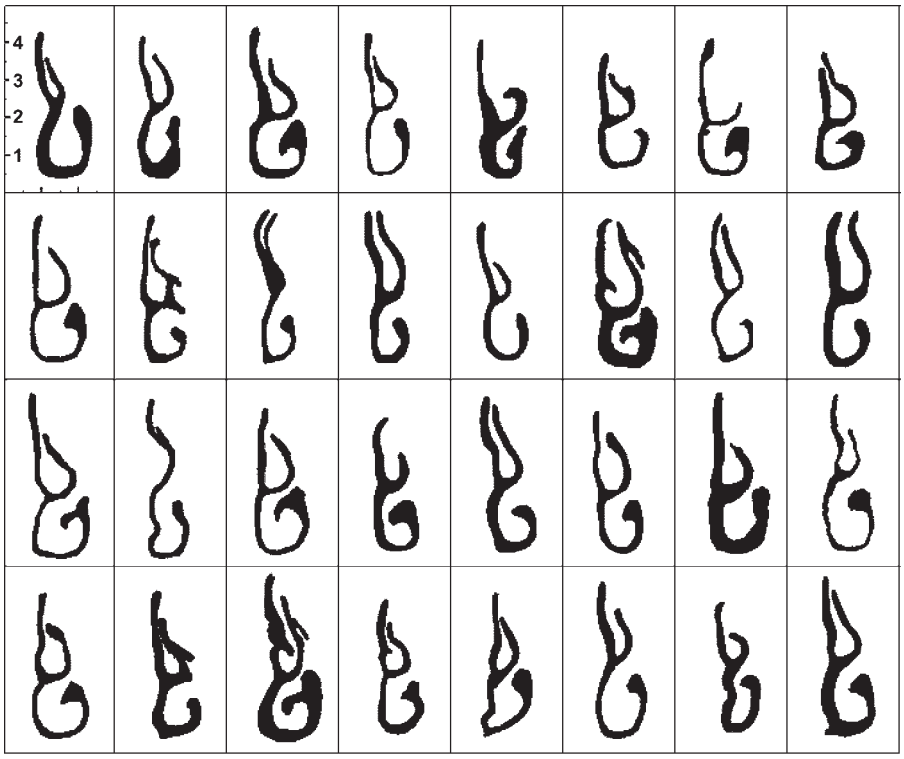

Fig. 9. Thirty-two of 60 nasal cavity cross-sectional shapes located 30 mm from the maxillary spine landmark. Scale at *top left* indicates cm.

shown in Fig. 10*B*. Because of the significant geometric variability at this location, the image in Fig. 10*B* is jagged and discontinuous. This example represents the worst case of the cross-sections, and at other locations with less variability the median image was quite smooth.

3) A separate "median-area" image was also generated at each cross-section using a different threshold value. This "auto-threshold" value was iteratively chosen so that that the CSA in the median-area image would match median CSA calculated from the up to 60 available images for that location. Figure 10*C* shows in red, the "median" image from *step 2* overlaid on top of the median-area image in yellow for $X = 30$ mm. The characteristic shape of the nasal airway at this location is now much more readily apparent.

4) Using the superimposed images it was possible to make minor manual edits to the shape of the cross-sectional image while constraining the area to match the median CSA of all available subject images. As shown in Fig. 10*D*, to further aid the final editing process, the Canny edge detection algorithm (5) was used to calculate and overlay the contours of the nasal cavity geometry from adjacent cross-sections. In Fig. 10*D*, the working contour at $X = 30$ mm is shown in yellow while the adjacent upstream contour at $X = 28$ mm is shown in green and the adjacent downstream contour at $X = 32$ mm is shown in red. These contours are overlaid on the median-area image, which is shown in blue. The final contour shapes at each cross-section were adjusted iteratively to avoid introduction of bias. In general, only very minor edits, if any, were required at most *X*-locations.

This procedure was employed for each of the 56 *X*-positions along the nasal cavity and 56 cross-sectional shapes for the standardized human nasal cavity were obtained (Fig. 11). At the nostril entry plane only, where there were less data available, the averaged physical descriptors (e.g., major and minor axis lengths in the nostril entry plane and angle between the major axis and base of nose) were calculated from the measured data (shown in Table 4), supplemented with the measured results of Kesavanathan and Swift (21). The combined averaged physical descriptors (current data merged with

Table 4. *Measurements of frontal/nostril regions from 7 sets of CT scans*

Subject No.	Sex	Length of Frontal Region in *X*-Direction, cm	Length Along Major Axis of Nostril at Inlet Plane, cm	Width Along Minor Axis of Nostril at Inlet Plane, cm	Nostril Angle, degrees	Internal Volume of Single Nasal Passage (Nostril to Choana), mm³		Surface area of Single Nasal Passage (Nostril to Choana, cm²	
						Left	Right	Left	Right
7	F	3.56	2.35	0.92	65.2	10.1	10.8	85.1	85.0
8	M	3.49	2.25	0.65	68.9	15.3	12.0	113.5	110.9
9	M	3.24	2.64	0.74	70.1	13.6	15.3	107.9	101.1
11	M	3.42	2.10	0.87	69.8	14.8	16.3	102.2	104.2
15	M	4.29	2.15	0.97	67.7	10.8	14.6	115.1	107.6
23	F	3.05	1.83	0.56	68.6	11.3	12.4	79.7	85.4
27	F	3.19	2.06	0.83	68.2	13.2	14.1	109.8	112.3
Average		3.46	2.2	0.79	68.4	13.2		101.4	
SD		0.41	0.25	0.15	1.6	2.0		12.3	
Max		4.29	2.64	0.97	70.1	16.3		115.1	
Min		3.05	1.83	0.56	65.2	10.1		79.7	

Downloaded from http://jap.physiology.org/ by 10.220.33.5 on January 25, 2017

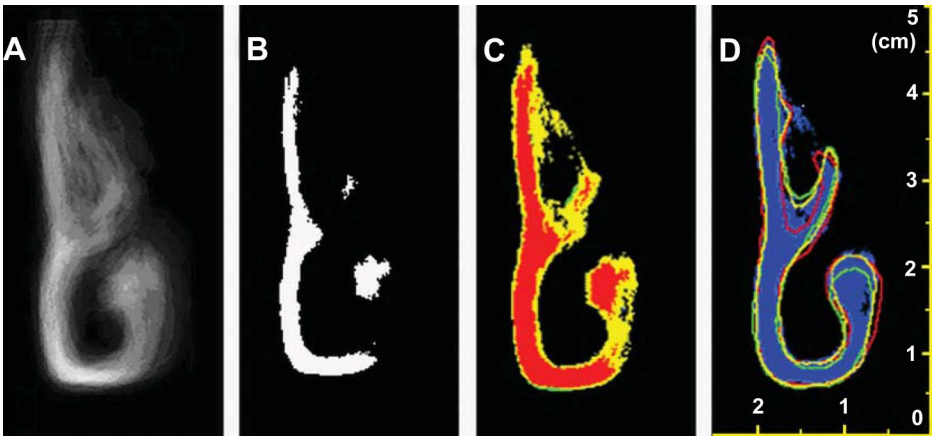

Fig. 10. Example coronal plane images at $X = 30$ mm obtained during processing to determine the characteristic cross-sectional geometry. *A*: ensemble averaged grayscale image; *B*: binarized 50% threshold ("median") image; *C*: median image in red overlaid on top of "median area" image in yellow; *D*: final boundaries of cavity at current *X*-position in yellow, at next upstream position in green, at next downstream position in red, overlaid on median area image in blue.

data from Ref. 21) at the nostril entry plane are shown in Table 5, and these values were used to define the shape of the inlet plane to the standardized nasal cavity model.

In the posterior region of the cavity, the two separate airways fuse into a single passageway at the choana, which spans the symmetry plane. Thus, as shown in Fig. 7, the number of available cross-sectional images suddenly drops from 60 to 30 at the merge point. However, since the goal of this work was to develop a single-sided nasal cavity model, and to remain consistent with the procedure developed above, the cross-sectional images past the choana were split and mirrored about the symmetry plane. In the final, standard cavity model detailed below, only one-half of the airway (patient's right side) is shown. Thus, if the final model were copied and mirrored, a full two-sided nasal cavity could easily be produced.

RESULTS

Construction of the Final Standardized Nasal Model

Similar to the generation of coarse models, all of the 56 final cross-sectional images were imported into 3D-Doctor and a coarse standardized nasal model was generated. This coarse standardized model was imported into ICEM and was smoothed using the same procedure described previously to create the final, standardized nasal model as shown in Fig. 12. The new model is referred to here and on figures as the Carleton-Civic standardized nasal model. Full geometric details of this model are freely available from Carleton University and may be downloaded for use by other researchers and clinicians at http://aerosol.mae.carleton.ca.

Analysis of the Carleton-Civic Standardized Nasal Model

Figure 13 shows the CSA of the standardized nasal model as a function of the distance from the maxillary spine landmark (selected here as the reference point), compared with the local, median, and averaged CSAs of all subjects used in this research. The values of CSA among the 60 nasal cavities vary significantly. However, the CSA of the new standardized geometry very closely tracks the median value of the CSA from all subject cavities, especially in the complex turbinate region. There is a slight deviation in the nostril region, ~2 cm upstream of the maxillary spine; however, the difference is insignificant relative to the variability among all models and is negligible when compared with the 14 complete nasal cavity models (Fig. 14).

Figure 14 shows CSAs of the standardized nasal cavity and the available 14 complete nasal passages, which allows a closer examination of the CSAs in the nostril region. Data are plotted as a function of distance relative to the tip of the nostril and without any geometric scaling to permit more critical comparison. The minimum CSA (MCA) of the nasal models occurs in a region 20–35 mm from the tip of nostril; the corresponding airway narrowing is called the nasal valve. For the standardized model, the MCA occurs at a location 24 mm from the nostril, which agrees very well with the averaged curves of 14 cavities. This is an additional indication that the standardized model effectively captures key geometrical features of the nasal cavity. The CSA then increases as expected in the region of the turbinates (35–75 mm from the nostril).

Figure 15 shows the CSA of the standardized nasal model as a function of the distance from the nostril, compared with available CSA data extracted from published literature. Both CT scan derived data [Min and Jang (31), Terheyden et al. (53), Kelly et al. (20)] and MRI derived data [Cheng et al. (7), Corey et al. (10)] are included. Data are plotted as *X*-position relative to the tip of the nostril using coordinate data as reported. It is important to note that some alignment bias would be expected among data in the literature in the absence of a common and rigorous alignment protocol. Because of the generally elongated shape of the nasal cavity, any relative misalignment about the *Y*- or *Z*-axes should bias toward higher estimates of CSA.

The scatter in the individual geometry data is again quite apparent; however, the standardized model correlates very well with all data at the anterior tip of the nasal passage, and there is a generally consistent trend among averaged data of multiple geometries. In particular, the standardized model CSA correlates well with the average data of four cavities from Cheng et al. (7) (where the reported CSA for the full two-sided cavities have been halved for comparison) and 12 single-sided cavities from Terheyden et al. (53). On careful observation, the standardized model trends on the lower side of the dispersed CSA values in Fig. 15. However, as the cited data from the literature are heavily biased toward male subjects (33 men/13 women) and the current data are slightly biased toward female subjects (13 men/17 women), this is not necessarily unexpected. The data from Min and Jang (31), which reflect an

Downloaded from http://jap.physiology.org/ by 10.220.33.5 on January 25, 2017

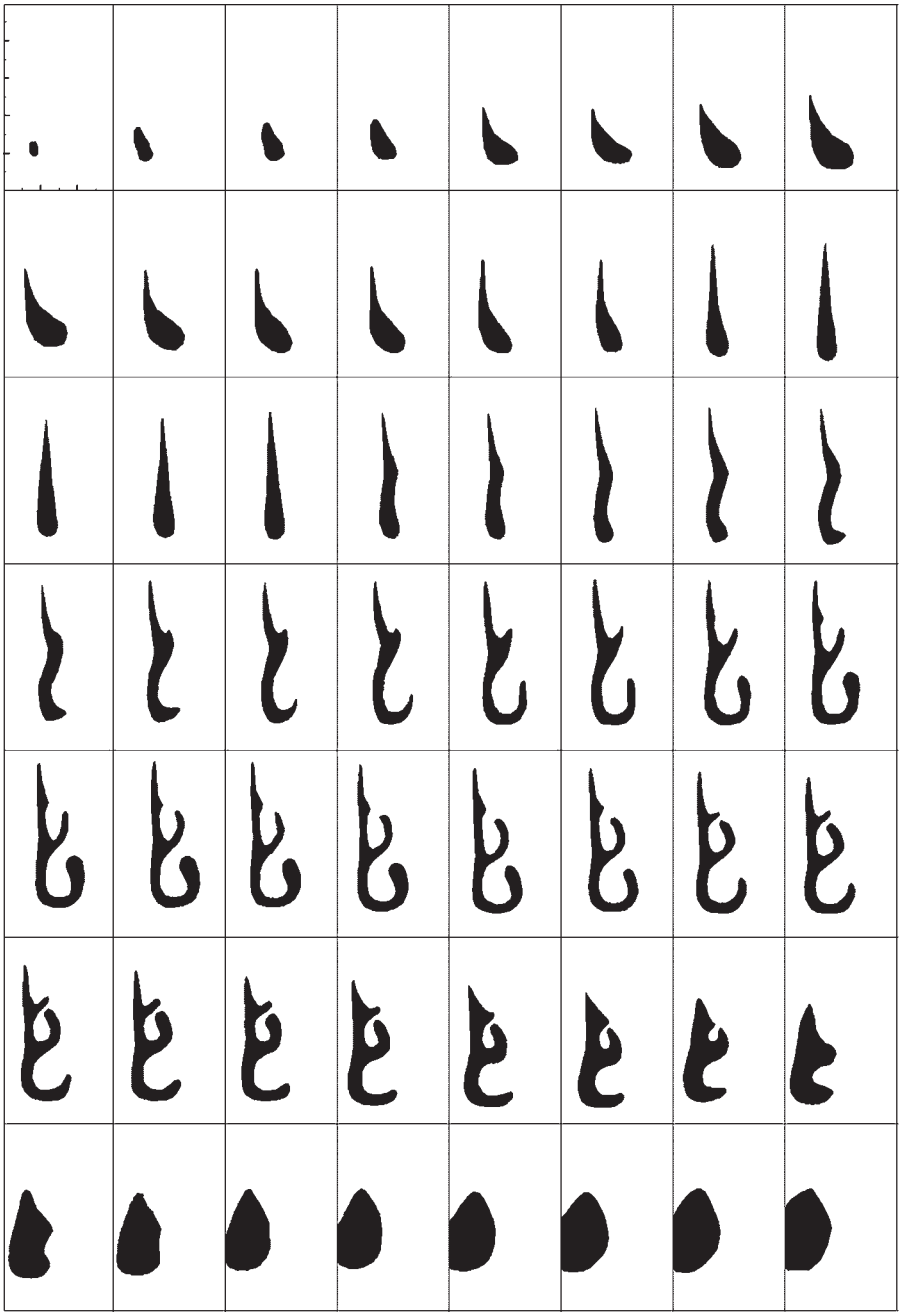

Fig. 11. Fifty-six cross-sectional shapes at 2-mm intervals along the *X*-axis of the standardized human nasal cavity. Scale markings at *top left* indicate cm.

identical sample size to the current study, do not seem to correlate as well with all of the other data. Although data from Min and Jang (31) span a narrower range, an overall flatter trend in CSA with distance is apparent. One could speculate that this difference may be attributable to differences in alignment (i.e., head pitch).

Table 5. *Averaged dimensions of the nostril inlet plane [merged raw data from Table 4 and from Kesavanathan and Swift (21)] compared with final values for the Carleton-Civic Standardized Model*

	Mean ± SD	Range	Standardized Model
Length of major axis	1.76±0.43 cm	1.18–2.64 cm	1.77
Width of minor axis	0.72±0.15 cm	0.50–0.97 cm	0.72
Nostril Angle	53±16.6°	17.5°–70.1°	67.7°

The internal volume and surface area of the standardized model (from tip to choana for a single passageway) were calculated as described above and were found to be 13.19 cm^3 and 90.69 cm^2, respectively. These values compare well with MRI measurements on 45 human subjects performed by Guilmette et al. (16), who reported mean nasal surface areas between 75.24 and 124.47 cm^2 (mean of 91.65 cm^2) and internal volumes between 7.37 and 16.91 cm^3 (mean of 8.9 cm^3).

In conclusion, a novel, standardized nasal cavity model has been generated using a novel procedure for aligning and processing 30 sets of CT scans of human nasal cavities. The

Downloaded from http://jap.physiology.org/ by 10.220.33.5 on January 25, 2017

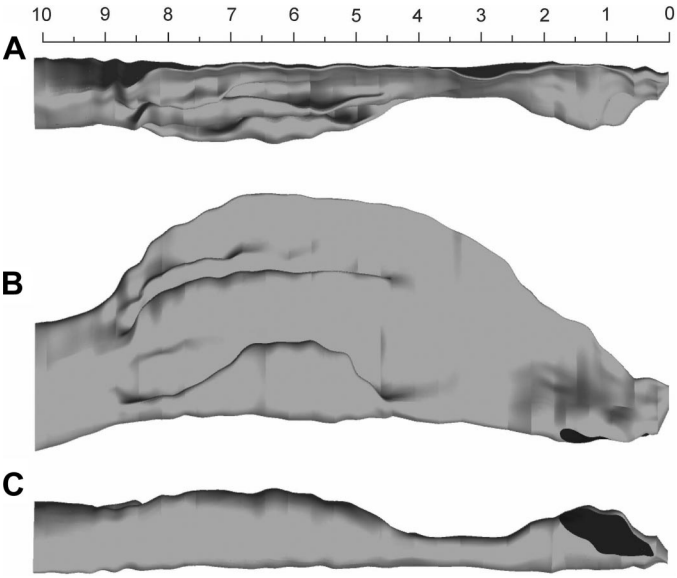

Fig. 12. Final Carleton-Civic standardized nasal cavity model. *A*: top view; *B*: side view; *C*: bottom view. Scale at top of image is in cm.

left and right nasal cavities were separately analyzed for each set of scans to give a total sample size of 60 individual cavities. The 60 cavities were rendered as 3-D digital models, and oriented, aligned, and scaled to allow an objective geometrical comparison. Through digital image processing, a standardized nasal cavity model was developed that closely matches the median CSA characteristic of the 60 raw geometries, while retaining the unique geometric features of the human nasal cavity.

This new model is freely distributed online through Carleton University and will be useful to researchers and physicians in a

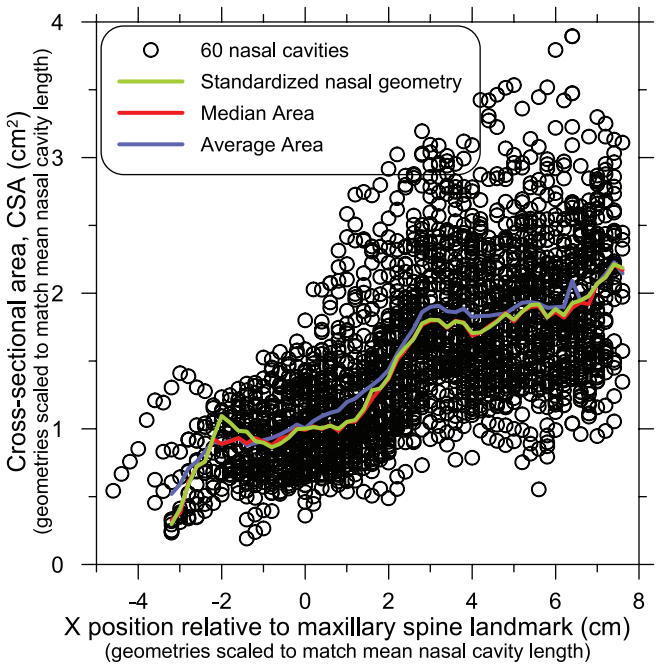

Fig. 13. Cross-sectional area of the Carleton-Civic standardized nasal model (green curve) compared with individual (dots), median (red curve), and average (blue curve) cross-sectional areas from all available subjects.

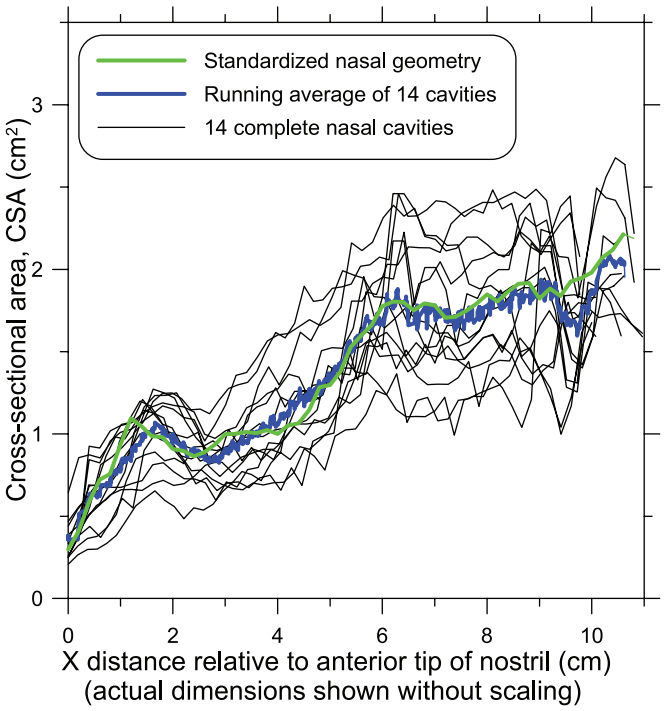

Fig. 14. Cross-sectional areas of the standardized nasal model (green curve) and 14 complete nasal passages (black curves). Running average of the 14 complete curves is shown for comparison in blue.

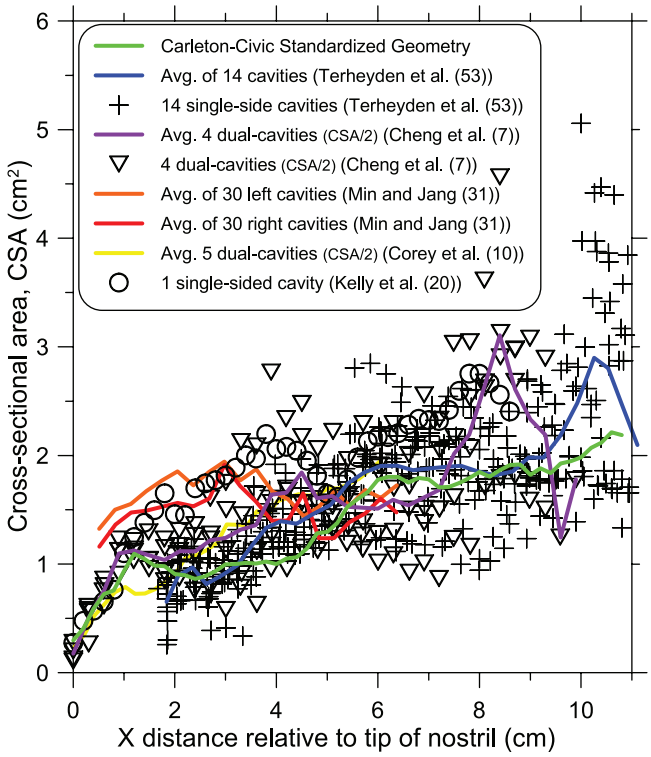

Fig. 15. Comparison of cross-sectional areas of the Carleton-Civic standardized nasal model (green curve) with published CT scan derived data from Min and Jang (31) (orange and red curves), Terheyden et al. (53) (crosses/blue curve), and Kelly et al. (20) (circles); and MRI derived data from Cheng et al. (7) (inverted triangles/purple curve) and Corey et al. (10) (yellow curve).

Downloaded from http://jap.physiology.org/ by 10.220.33.5 on January 25, 2017

variety of fields. In addition, the model could serve as a candidate standard for aerosol deposition testing in the pharmaceutical industry, enabling more accurate experimental and numerical predictions of pharmaceutical aerosol deposition and raising possibilities for new insight, faster development, and reduced costs of better drug delivery devices. As a diagnostic tool, the CT scan of a patient could be processed and compared against this standardized model to indicate deviation from the present average characteristic values, such as CSA, nostril area, or general shape. Finally, the specific procedure developed in this study could be applied in comprehensive studies involving different identifiable groups in the population, as more CT scan or MRI data become available.

GRANTS

This work was supported by the Natural Sciences and Engineering Research Council of Canada. Ms. Liu was supported by an Ontario Graduate Scholarship.

REFERENCES

1. **Adamson JE.** Constriction of the internal nasal valve in rhinoplasty: treatment and prevention. *Ann Plastic Surg* 18: 114–121, 1987.
2. **Bateman ND, Whymark AD, Clifton NJ, Woolford TJ.** A study of intranasal distribution of azelastine hydrochloride aqueous nasal spray with different spray techniques. *Clin Otolaryngol* 27: 327–330, 2002.
3. **Bennett WD, Zeman KL.** Effect of race on fine particle deposition for oral and nasal breathing. *Inhalation Toxicol* 17: 641–648, 2005.
4. **Canada's Ethnocultural Mosaic.** 2006 Census. *Statistics Canada*, Catalogue No. 97–562-X, April 2008.
5. **Canny J.** A Computational Approach to Edge Detection. *IEEE Trans Pattern Analysis Machine Intell* 8: 679–714, 1986.
6. **Cheng KH, Cheng YS, Yeh HC, Guilmette RA, Simpson SQ, Yang YH, Swift DL.** In vivo measurements of nasal airway dimensions and ultrafine aerosol deposition in the human nasal and oral airways. *J Aerosol Sci* 27: 785–801, 1996.
7. **Cheng YS, Yeh HC, Guilmette RA, Simpson SQ, Cheng KH, Swift DL.** Nasal deposition of ultrafine particles in human volunteers and its relationship to airway geometry. *Aerosol Sci Technol* 25: 274–291, 1996.
8. **Cheng YS.** Aerosol deposition in the extra-thoracic region. *Aerosol Sci Technol* 37: 659–671, 2003.
9. **Churchill SE, Shackelford LL, Georgi JN, Black MT.** Morphological variation and airflow dynamics in the human nose. *Am J Human Biol* 16: 625–638, 2004.
10. **Corey JP, Gunfor A, Nelson R, Fredberg J, Lai V.** A comparison of the nasal cross-sectional areas and volumes obtained with acoustic rhinometry and magnetic resonance imaging. *Otolaryngol Head Neck Surg* 117: 349–354, 1997.
11. **Damm M, Vent J, Schmidt M, Theissen P, Eckel HE, Lötsch J, Hummel T.** Intranasal volume and olfactory function. *Chem Senses* 27: 831–839, 2002.
12. **Davis SS, Eccles R.** Nasal congestion: mechanisms, measurement and medications. Core information for the clinician. *Clin Otolaryngol* 29: 659–666, 2004.
13. **De Boor C.** *A Practical Guide to Splines*. Berlin: Springer-Verlag, 1978.
14. **Fidone SJ, Gonzalez C.** Initiation and control of chemoreceptor activity in the carotid body. *Handbook of Physiology. The Respiratory System. Control of Breathing.* Bethesda, MD: Am Physiol Soc, 1986, sect. 3, vol. II, pt. 1, chapt. 9, p. 247–261.
15. **Frey WH.** Intranasal delivery: bypassing the blood-brain barrier to deliver therapeutic agents to the brain and spinal cord. *Drug Del Technol* 2: 46–49, 2002.
16. **Guilmette RA, Cheng YS, Griffith WC.** Characterising the variability in adult human nasal airway dimensions. *Ann Occupational Hygiene* 41: 491–496, 1997.
17. **Hilberg O, Jackson AC, Swift DL, Pedersen OF.** Acoustic rhinometry: evaluation of nasal cavity geometry by acoustic reflection. *J Appl Physiol* 66: 295–303, 1989.
18. **Illum L.** Transport of drugs from the nasal cavity to the central nervous system. *Eur J Pharm Sci* 11: 1–18, 2000.
19. **Inthavong K, Tian ZF, Li HF, Tu JY, Yang W, Xue CL, Li CG.** A numerical study of spray particle deposition in a human nasal cavity. *Aerosol Sci Technol* 40: 1034–1033, 2006.
20. **Kelly JT, Prasad AK, Wexler AS.** Detailed flow patterns in the nasal cavity. *J Appl Physiol* 89: 323–337, 2000.
21. **Kesavanathan J, Swift DL.** Human nasal passage particle deposition: the effect of particle size, flow rate and anatomical factors. *Aerosol Sci Technol* 28: 457–463, 1998.
22. **Keyhani K, Scherer PW, Mozell MM.** Numerical simulation of airflow in the human nasal cavity. *J Biomech Eng* 117: 429–441, 1995.
23. **Kim SK, Chung SK.** An investigation on airflow in disordered nasal cavity and its corrected models by tomographic PIV. *Measurement Sci Technol* 15: 1090–1096, 2004.
24. **Kimbell JS, Subramaniam RP, Gross EA, Schlosser PM, Morgan KT.** Dosimetry modeling of inhaled formaldehyde: comparisons of local flux predictions in the rat, monkey, and human nasal passages. *Toxicol Sci* 64: 100–110, 2001.
25. **Kimbell JS.** Nasal dosimetry of inhaled gases and particles: where do inhaled agents go in the nose? *Toxicol Pathol* 34: 270–273, 2006.
26. **Kramer PR, Wray S.** Novel gene expressed in nasal region influences outgrowth of olfactory axons and migration of luteinizing hormone releasing hormone (LHRH) neurons. *Genes Dev* 14: 1824–1834, 2000.
27. **Lenders H, Pirsig W.** Diagnostic value of acoustic rhinometry: patients with allergic and vasomotor rhinitis compared with normal controls. *Rhinology* 28: 5–16, 1990.
28. **Liu Y, Matida EA, Gu J, Johnson MR.** Numerical simulation of aerosol deposition in a 3-D human nasal cavity using RANS, RANS/EIM, and LES. *J Aerosol Sci* 38: 683–700, 2007.
29. **Mathison S, Nagilla R, Kompella UB.** Nasal route for direct delivery of solutes to the central nervous system: fact or fiction? *J Drug Target* 5: 413–441, 1998.
30. **Marieb EN.** *Human Anatomy and Physiology*. Menco Park, CA: Benjamin/Cummings, 1995.
31. **Min YG, Jang YJ.** Measurements of cross-sectional area of the nasal cavity by acoustic rhinometry and CT scanning. *Laryngoscope* 105: 757–759, 1995.
32. **Minn A, Leclerc S, Heydel JM, Minn AL, Denizot C, Cattarelli M, Netter P, Gradinaru D.** Drug transport into the mammalian brain: the nasal pathway and its specific metabolic barrier. *J Drug Target* 10: 285–296, 2002.
33. **Murry DP, ELHakim H, Ahsan F, Nunez DA.** Does synchronous nasal surgery increase the risk of postoperative haemorrhage in adult patients undergoing tonsillectomy? *J Laryngol Otol* 117: 707–709, 2003.
34. **O'Neill G, Tolley NS.** Theoretical considerations of nasal airflow mechanics and surgical implications. *Clin Otolaryngol* 13: 273–277, 1998.
35. **Overton JH, Kimbell JS, Miller FJ.** Dosimetry modeling of inhaled formaldehyde: the human respiratory tract. *Toxicol Sci* 64: 122–134, 2001.
36. **Pang KP.** One-stage nasal and multi-level pharyngeal surgery for obstructive sleep apnoea: safety and efficacy. *J Laryngol Otol* 119: 272–276, 2005.
37. **Raj P, Stableforth DE, Morgan DW.** A prospective study of nasal disease in adult cystic fibrosis. *J Laryngol Otol* 114: 260–263, 2000.
38. **Rajagopal MR, Jerry P.** Applied anatomy and physiology of the airway and breathing. *Indian J Anaesth* 49: 251–256, 2005.
39. **Reber M, Rahm F, Monnier P.** The role of acoustic rhinometry in the pre- and postoperative evaluation of surgery for nasal obstruction. *Rhinology* 36: 184–187, 1998.
40. **Rhomberg LR, Lewandowski TA.** Methods for identifying a default cross-species scaling factor. *Human Ecological Risk Assessment* 12: 1.94–1127, 2006.
41. **Roberts ES, Wong VA, McManus BE, Marshall MW, Lancianese S, Dorman DC.** Changes in intracellular pH play a secondary role in hydrogen sulfide-induced nasal cytoxicity. *Inhalation Toxicol* 18: 159–167, 2006.
42. **Roush GC.** Epidemiology of cancer of the nose and paranasal sinuses: general concepts. *Head Neck Surg* 2: 3–11, 1979.
43. **Sarkar MA.** Drug metabolism in the nasal mucosa. *Pharm Res* 9: 1–9, 1992.
44. **Saunders MW, Jones NS, Kabala JE.** Parameters of nasal airway anatomy on magnetic resonance imaging correlate poorly with subjective symptoms of nasal patency. *Clin Otolaryngol Appl Sci* 24: 431–434, 1999.
45. **Schroeter JD, Kimbell JS, Asgharian B.** Analysis of particle deposition in the turbinate and olfactory regions using a human nasal computational fluid dynamics model. *J Aerosol Med-Deposition Clearance Effects Lung* 19: 301–313, 2006.
46. **Schroeter JD, Kimbell JS, Gross EA, Willson GA, Dorman DC, Tan YM, Clewell HJ III.** Application of physiological computational fluid dynamics models to predict interspecies nasal dosimetry of inhaled Acrolein. *Inhalation Toxicol* 20: 227–243, 2008.
47. **Subramaniam RP, Richardson RB, Morgan KT, Kimbell JS, Guilmette RA.** Computational fluid dynamics simulations of inspiratory air-

Downloaded from http://jap.physiology.org/ by 10.220.33.5 on January 25, 2017

flow in the human nose and nasopharynx. *Inhalation Toxicol* 10: 91–120, 1998.
48. **Sullivan M.** Rhinoscopy: a diagnostic aid? *J Small Animal Practice* 28: 839–843, 1987.
49. **Suman JD, Laube BL, Dalby R.** Comparison of nasal deposition and clearance of aerosol generated by a nebulizer and aqueous spray pump. *Pharm Res* 16: 1648–1652, 1999.
50. **Suman JD, Laube BL, Lin T, Brouet G, Dalby R.** Relevance of in vitro tests of nasal solutions to predict in vivo deposition. *Pharm Res* 19: 1–6, 2002.
51. **Suzina AH, Hamzah M, Samsudin AR.** Objective assessment of nasal resistance in patients with nasal disease. *J Laryngol Otology* 114: 260–263, 2000.
52. **Swift DL, Kesavanathan J.** The anterior human nasal passage as a fibrous filter for particles. *Chem Engineer Comm* 151: 65–78, 1996.
53. **Terheyden H, Maune S, Mertens J, Hilberg O.** Acoustic rhinometry: validation by three-dimensionally reconstructed computer tomographic scans. *J Appl Sci* 89: 1013–1021, 2000.
54. **Tian ZF, Inthavong K, Tu JY.** Deposition of inhaled wood dust in the nasal cavity. *Inhal Toxicol* 19: 1155–1165, 2007.
55. **Wang DY, Goh DYT, Ho AKL, Chew FT, Yeoh KH, Lee BW.** The upper and lower airway responses to nasal challenge with house-dust mite Blomia tropicalis. *Allergy* 58: 78–82, 2003.
56. **Weinhold I, Mlynski G.** Numerical simulation of airflow in the human nose. *Eur Arch Otorhinolaryngol* 261: 452–455, 2004.
57. **Yu G, Zhang Z, Lessman R.** Fluid flow and particle diffusion in the human upper respiratory system. *Aerosol Sci Technol* 28: 146–158, 1998.
58. **Zhao K, Pribitkin EA, Cowart BJ, Rosen D, Scherer PW, Dalton P.** Numerical modeling of nasal obstruction and endoscopic surgical intervention: outcome to airflow and olfaction. *Am J Rhinol* 20: 308–316, 2006.
59. **Zhao K, Scherer PW, Hajiloo SA, Dalton P.** Effect of anatomy on human nasal air flow and odorant transport patterns: implications for olfaction. *Chem Senses* 29: 365–379, 2004.

Downloaded from http://jap.physiology.org/ by 10.220.33.5 on January 25, 2017